Eur. Phys. J. D (2024) 78:105
https://doi.org/10.1140/epjd/s10053-024-00897-5

THE EUROPEAN PHYSICAL JOURNAL D

Regular Article

Radiative and opacity data obtained from large-scale atomic structure calculations and from statistical simulations for the spectral analysis of kilonovae in their photospheric and nebular phases: the sample case of Er III

Jérôme Deprince[1,2,a], Helena Carvajal Gallego[1,b], Sirine Ben Nasr[1,c], Lucas Maison[1,d], Jean-Christophe Pain[3,4,e], Patrick Palmeri[1,f], and Pascal Quinet[1,5,g]

[1] Physique Atomique et Astrophysique, Université de Mons, 7000 Mons, Belgium
[2] Institut d'Astronomie et d'Astrophysique, Université Libre de Bruxelles, 1050 Brussels, Belgium
[3] CEA, DAM, 91297 Arpajon, France
[4] Laboratoire Matière en Conditions Extrêmes, CEA, Université Paris-Saclay, 91680 Bruyères-le-Châtel, France
[5] IPNAS, Université de Liège, Sart Tilman, 4000 Liège, Belgium

Received 30 March 2024 / Accepted 11 July 2024 / Published online 13 August 2024

Abstract. This study is an overview of the atomic data and opacity computations performed by the Atomic Physics and Astrophysics Unit of Mons University in the context of kilonova emission following neutron star mergers, in both the photospheric and nebular phases. In this work, as a sample case, we focus on a specific lanthanide ion, namely Er III. As far as the LTE photospheric phase of the kilonova ejecta is concerned, we present our calculations using both a theoretical method (the pseudo-relativistic Hartree-Fock method, HFR) and a statistical approach (the Resolved Transition Array approach, RTA) to obtain the atomic data required to estimate the Er III expansion opacity for typical conditions expected in kilonova ejecta one day after the merger. In order to draw the limitations of both of our strategies, the results obtained using the latter are compared, and a calibration procedure of the HFR atomic data in this context is also discussed. Concerning the kilonova ejecta nebular phase, atomic parameters that characterize forbidden lines in Er III are calculated using HFR as well as another computational approach, namely the Multiconfiguration Dirac–Hartree–Fock (MCDHF) method. The potential detection of such lines in late-phase kilonova spectra is then discussed.

1 Introduction

Since the first detection of gravitational waves originating from the merger of two neutron stars (NS), known as the GW170817 event [1], and its electromagnetic counterpart, called kilonova AT 2017gfo, the study of the atomic structures and the radiative parameters characterizing the heavy elements of the periodic table has experienced a significant resurgence. This is mainly due to the fact that these heavy elements, i.e., heavier than iron, are abundantly produced by the nucleosynthesis r-process in the material ejected following the NS coalescence [2].

Most heavy elements have a fairly complex atomic structure, in particular the lanthanides ($Z = 57 - 71$) and the actinides ($Z = 89 - 103$) which present electronic configurations in which the 4f or 5f subshell is partially filled, giving rise to numerous energy levels and therefore many possible radiative transitions between these energy levels. Consequently, in the kilonova photospheric phase, i.e., in the first few days after the merger, the spectrum is greatly affected by a significant opacity due to the absorption of light by millions of electric dipole transitions (E1) belonging to the different heavy ions present in the ejecta [2]. At later times, as the NS merger ejecta continues to expand, temperatures and densities decrease rapidly, leading to non-local thermodynamic equilibrium (NLTE) conditions at which the kilonova is considered to be in the nebular phase. This has the consequence that the spectrum is then emission line dominated, unlike the quasi-

[a] e-mail: jerome.deprince@umons.ac.be (corresponding author)
[b] e-mail: helena.carvajalgallego@umons.ac.be
[c] e-mail: sirine.bennasr@umons.ac.be
[d] e-mail: lucas.maison@umons.ac.be
[e] e-mail: jean-christophe.pain@cea.fr
[f] e-mail: patrick.palmeri@umons.ac.be
[g] e-mail: pascal.quinet@umons.ac.be

blackbody continuum spectrum observed in the photospheric phase. Moreover, the infrared nebular phase kilonova spectrum detected by the *Spitzer Space Telescope* was assumed by Kasliwal et al. [3] to contain forbidden lines of magnetic (M1) and electric quadrupole (E2) types. The key role of such forbidden transitions in kilonova modeling was also underlined by Gillanders et al. [4] who showed how the inclusion of M1 and E2 lines of heavy elements could lead to the identification of elemental signatures through radiative transfer calculations, while emphasizing the lack of accurate atomic data available for these lines in order to perform reliable kilonova spectral analyses.

For these reasons, during the last years, numerous studies of atomic structures and radiative parameters in heavy elements have been pursued essentially with the aim of determining the opacities affecting the spectra of kilonovae. It would be tedious to make an exhaustive list of these previous works here but, if we limit ourselves to lanthanide ions, we can mention those related to La V-X [5], Ce II-IV [6], Ce IV [7], Ce V-X [8], Pr IV [9], Pr-Gd II [10], Pr-Nd-Pm V-X [11], Nd II-IV [12,13], Sm V-X [14], Tb-Yb II [15], Er III [16], and Lu V [17]. All lanthanide atoms from I to IV charge stages and the corresponding opacities were also studied by [18], while the atomic data and opacity calculations were performed for three selected lanthanides (Nd, Sm, Eu) and for all the elements from La to Ra, thus including the lanthanides ionized to the states V - XI, by Banerjee et al. [19] and Banerjee et al. [20], respectively. To all these works must be added our recent investigation of forbidden lines in Nd III for spectral analysis of nebular phase kilonovae [21].

In the present paper, we give an overview of the atomic data calculations performed by the Atomic Physics and Astrophysics Unit of Mons University (Belgium) for the spectral analysis of kilonovae in their photospheric and nebular phases. To do this, the particular case of a specific lanthanide ion, namely doubly ionized erbium, Er III, was chosen. More precisely, in the case of the photospheric phase, we show how atomic data obtained from a computational method based on the pseudo-relativistic Hartree–Fock (HFR) theoretical approach, as well as from a statistical method based on the Resolved Transition Array (RTA) approximation, can be used to obtain expansion opacities, by focusing the discussion on the respective advantages and limitations of these two approaches. Then, for the nebular phase spectral analysis, we provide new radiative decay rates for the forbidden lines, i.e., magnetic dipole (M1) and electric quadrupole (E2) lines, involving the experimentally known energy levels within the $4f^{12}$ ground configuration of Er III obtained by means of two independent theoretical methods, namely HFR and the fully relativistic multiconfiguration Dirac–Hartree–Fock (MCDHF) methods. The comparison between these two approaches making it possible to evaluate the reliability of the results obtained and to predict the possible presence of [Er III] lines in the observed kilonova spectra.

2 Methods used for calculating atomic data

2.1 Pseudo-relativistic HFR computational approach

The pseudo-relativistic Hartree–Fock method (HFR) was developed by Cowan [22] to compute atomic structures and properties based on the Schrödinger equation. In this approach, a set of orbitals is obtained for each configuration included in the model by solving the Hartree–Fock (HF) equations, which arise from a variational principle applied to each configuration average energy. Some relativistic corrections are also included in a perturbative way, namely the Blume–Watson spin–orbit interaction, the mass-variation correction and the one-body Darwin term. The self-consistent field method is then used to solve the coupled integro-differential HF equations.

Based on the Slater–Condon theory, the atomic wavefunctions (i.e., the Hamiltonian eigenfunctions) are built as a superposition of basis wavefunctions. In the $LSJ\pi$ representation, they read as

$$\Psi(\gamma JM_J P) = \sum_i^{N_{\mathrm{CSF}}} c_i \, \phi(\gamma_i L_i S_i JM_J P). \tag{1}$$

In the HFR method, the non-orthogonality between orbitals belonging to different configurations is thus disregarded.

The multiconfiguration Hamiltonian matrix is constructed and diagonalized following the Slater–Condon theory, i.e., each matrix element is obtained by a sum of products of Racah angular coefficients and radial Slater and spin–orbit integrals as

$$\langle i|H|j\rangle = \sum_l v_{ij}^l x_l. \tag{2}$$

In the present computation, scaling factors of 0.85 were applied to the Slater integrals as recommended by Cowan [22] in order to take the interactions with configurations not included in the model into account. Nevertheless, this choice is not crucial for the purpose of this work since Carvajal Gallego et al. [11] recently showed that scaling factor values between 0.80 and 0.95 does not affect the expansion opacities computed with the corresponding HFR data. Finally, the radiative wavelengths and oscillator strengths for all possible transitions are calculated using the eigenvalues and eigenstates obtained by means of this method.

It is important to remember here that the HFR approach is particularly well suited to the determination of opacities because the latter requires the use of a very large number of radiative data of similar quality for all the transitions considered in the calculation. This is precisely the case of the HFR method since, in this approach, all the configurations of the model satisfy a variational minimum and can thus all be considered as spectroscopic, unlike most other multi-configurational theoretical methods which generally call on a model

with spectroscopic configurations and correlation configurations, therefore leading to a set of radiative data which may be of different quality depending on the configurations involved in the transitions.

2.2 Fully relativistic MCDHF computational approach

The second theoretical method used in this work to model the atomic structure of doubly ionized erbium is the `Multiconfiguration Dirac-Hartree-Fock` method (`MCDHF`) described by Grant [23]. All the `MCDHF` computations were done using the `GRASP2018` package [24], that is the latest version of the General Relativistic Atomic Structure Program (GRASP). In the `MCDHF` approach, the starting point is the Dirac–Coulomb Hamiltonian

$$H_{DC} = \sum_{i=1}^{N} (c\boldsymbol{\alpha}_i.\mathbf{p}_i + (\beta_\mathbf{i} - 1)c^2 + V_{\text{nucl}}(r_i)) + \sum_{i>j} \frac{1}{r_{ij}}, \tag{3}$$

where $V_{\text{nucl}}(r_i)$ is the monopole part of the electron–nucleus Coulomb interaction, r_{ij} is the distance between electrons i and j, α and β are the 4×4 Dirac matrices, and c is the speed of light.

The solutions to the wave equations are referred to as atomic state functions (ASFs), $\Psi(\gamma PJ)$, which are represented by linear combinations of configuration state functions (CSFs), $\Phi(\gamma_j PJ)$:

$$\Psi(\gamma JM_J P) = \sum_{j=1}^{N_{\text{CSF}}} c_j \Phi(\gamma_j JM_J P), \tag{4}$$

where P is the parity and J is the total angular momentum. γ_j represents all necessary quantum numbers and the orbital occupancy to define the CSF, while c_j are the mixing coefficients.

The CSFs are in turn constructed as angular-momentum-coupled, anti-symmetrized products of one-electron Dirac-orbitals of the form

$$\Psi_{n\kappa m}(r, \theta, \phi) = \frac{1}{r} \begin{pmatrix} P_{n\kappa}(r)\chi_{\kappa m}(\theta, \phi) \\ iQ_{n\kappa}(r)\chi_{-\kappa m}(\theta, \phi) \end{pmatrix}, \tag{5}$$

where $P_{n\kappa}(r)$ and $Q_{n\kappa}(r)$ are the large and small components of the radial wave function and where $\chi_{\pm\kappa m}$ $(\theta,\ \phi)$ are two-component spin–orbit functions with $\kappa = -(l + 1)$ for $j = l + 1/2$ and $\kappa = l$ for $j = l - 1/2$.

The radial parts of the wavefunctions and the expansion coefficients c_j are optimized iteratively in the optimal level (OL/EOL) mode using a self-consistent field method. Finally, expansion coefficients are obtained through the diagonalization of the Dirac–Coulomb Hamiltonian in a relativistic configuration interaction (RCI) computation. This RCI computational step also enables the inclusion of the Breit transverse–photon interaction and QED corrections such as the self-energy and vacuum polarization effects.

Note that the `MCDHF` method is more suited to the calculation of radiative transitions involving a limited number of levels, that is to say those on which the optimization of the orbitals is carried out, the other states being to be considered as correlation states since the set of orbitals is identical for all the configuration state functions of the model.

2.3 RTA statistical approach

The statistical Resolved Transition Array (RTA) method was first proposed by Bauche et al. [25] and detailed in Bauche et al. [25,26]. In this method, the diagonalization of the Hamiltonian matrix is replaced by a set of compact statistical formulae where only the set of radial wave equations is solved for each electronic configuration to determine all the needed radial integrals and parameters. Carvajal Gallego et al. [27] very recently showed that this method allows the computation of reliable expansion opacities in moderately charged lanthanide ions such as Sm VIII, Eu VI and Dy VIII. In that paper, the main tools to obtain the energy levels, transition wavelengths and oscillator strengths needed for the expansion opacity computation were already presented in detail [27] and we provide here only a brief description.

For each configuration C considered in our model, $N_C(J)$ energy levels, E, are drawn randomly for each total quantum number J using their corresponding statistical distribution approximated by a Gaussian:

$$D_C(E) = \frac{N_C}{2\pi\sqrt{v_C}} \exp\left[-\frac{(E - E_{av})^2}{2v_C}\right], \tag{6}$$

where $N_C = \sum_J N_C(J)$ is the total number fine structure levels of the configuration C, as computed from Eqs. (2,3) in Carvajal Gallego et al. [27], and E_{av} its average energy as determined in this work by solving the radial HFR equations [22] and v_C is the variance of the distribution which is computed from compact formulae tabulated, e.g., in Table 3.2 in Bauche et al. [26].

From these random energies E_l and E_u drawn, respectively, in the lower C_l and upper C_u configuration of each electric dipole (E1) transition array $C_l - C_u$, the wavelengths, λ_{lu}, of $L(C_l - C_u)$ transitions that obey the E1 selection rules are determined as

$$\lambda_{lu} = \frac{1}{\sigma_{lu}} = \frac{hc}{(E_u - E_l)}, \tag{7}$$

where the total number of E1 transitions of a $C_l - C_u$ array, $L(C_l - C_u)$, is calculated [26] as follows:

$$L(C_l - C_u) = \frac{3}{\sqrt{8\pi}} g(C_l)g(C_u) \left[v_M(C_l) + v_M(C_u)\right]^{-3/2} \times \left[1 - \frac{1}{v_M(C_l) + v_M(C_u)}\right], \tag{8}$$

where $g(C_u)$ and $g(C_l)$ are, respectively, the degeneracies of the upper and the lower configurations [22] of the $C_u - C_l$ array, and $v_M(C_u)$ and $v_M(C_l)$ are their respective variances of their distributions of magnetic quantum number M [26].

Concerning the weighted oscillator strength, $g_l f_{lu}$, it is determined for each E1 transition of the $C_l - C_u$ transition array by [22]:

$$g_l f_{lu} = (3.0376 \times 10^{-6})\, \sigma_{lu}\, S_{lu}, \tag{9}$$

where g_l is the statistical weight of the lowest level E_l of the transition, the wavenumber $\sigma_{lu} = E_u - E_l$ is given in cm^{-1}, and the line strength S_{lu} in a.u. The latter is obtained by $S_{lu} = \xi(C_l - C_u) a_{lu}^2$ using a random value of the line amplitude a_{lu} [25] and a normalization factor $\xi(C_l - C_u)$ which is related to the total strength $S(C_l - C_u)$ of the $C_l - C_u$ array [26]:

$$\begin{aligned} &S(C_l - C_u) \\ &= S\left(n_1 \ell_1^{N_1+1} n_2 \ell_2^{N_2} n_3 \ell_3^{N_3} - n_1 \ell_1^{N_1} n_2 \ell_2^{N_2+1} n_3 \ell_3^{N_3}\right) \\ &= 2\ell_> \binom{4\ell_1 + 1}{N_1} \binom{4\ell_2 + 1}{N_2} \binom{4\ell_3 + 2}{N_3} [D(n_1\ell_1, n_2\ell_2)]^2, \end{aligned} \tag{10}$$

where $n_i \ell_i$ are open subshells, $\ell_>$ is the greater value between ℓ_1 and ℓ_2 and $D(n_1\ell_1, n_2\ell_2)$ is the electric dipole (E1) radial integral of r between the central-field monoelectronic radial function $P_{n_1\ell_1}(r)$ and $P_{n_2\ell_2}(r)$ as determined by solving the radial equation.

Regarding the transition amplitudes a_{lu}, they are randomly drawn in a Gaussian distribution with a mean at zero a.u. and a variance, v_a, correlated with the transition wavenumber, σ_{lu}, from the following expression [25]:

$$\ln(v_a) = \alpha + \beta\, |\sigma - \sigma_{av}|, \tag{11}$$

where σ is the average of the bin boundaries $\sigma = (\sigma_1 + \sigma_2)/2$ where the values of σ_{lu} are distributed into consecutive bins of equal widths in both sides of σ_{av}, the average wavenumber of the unresolved transition array (UTA) $C_l - C_u$. The latter can be split into several peaks called spin-orbit-split arrays (SOSA) when the spin–orbit interaction becomes large and, consequently, the same simulation has to be performed for each SOSA separately [26]. The correlation parameters α and β that appear in Eq. (11) can be computed via the resolution of the following equations [25]. The solution of the following implicit equation supplies the value of β:

$$\left(x^2 + 1 - \frac{v_w}{v_{un}}\right) \exp\left(\frac{x^2}{2}\right) \mathrm{erfc}\left(\frac{x}{\sqrt{2}}\right) = x\sqrt{\frac{2}{\pi}}, \tag{12}$$

where $x = -\beta\sqrt{v_{un}}$, while the value of α is derived from that of x and from the average strength of the $C_l - C_u$ array, $S_{av}(C_l - C_u)$, as below:

$$\begin{aligned} \alpha = &\ln\left[S_{av}(C_l - C_u)\right] + \ln\left(x^2 + 1 - \frac{v_w}{v_{un}}\right) \\ &- \ln(x) + \frac{1}{2}\ln\left(\frac{\pi}{2}\right), \end{aligned} \tag{13}$$

where $S_{av}(C_l - C_u) = S(C_l - C_u)/L(C_l - C_u)$.

In Eqs. (12,13), the weighted variance of the line wavenumber σ_{lu} by the corresponding line strength S_{lu}, v_w, and the corresponding unweighted variance, v_{un}, can be determined by compact formulae for a $C_l - C_u$ UTA [28–32].

3 Kilonova photospheric phase: expansion opacities

3.1 HFR atomic data calculations

In this section, we describe our HFR atomic data computation in order to determine the opacity of Er III and make some comparisons with existing data. In particular, we discuss the importance of a calibration procedure that improves atomic data in the context of opacity calculations for kilonova modeling purpose.

The HFR atomic model that we chose to compute the atomic structure and radiative parameters for Er III is justified based on the same strategy used for Nd II, Nd III, U II and U III in [13], in which we discussed the importance of the multiconfiguration model choice. In the aforementioned paper, we showed that converged opacities can be obtained with HFR atomic models including configurations built by considering single excitations from the ground configuration to all $n = 5$ and $n = 6$ orbitals as well as selected double electron excitations toward 5d, 6s and 6p subshells. We demonstrated that using such HFR multiconfiguration models was sufficient to capture the bulk of the atomic opacities, both around the peak and the tail [13]. In the present case of Er III, whose observed ground configuration is $4f^{12}$, the corresponding configuration list considered is the following: $4f^{12}$, $4f^{11}$ {5d,5f,5g,6s,6p,6d,6f,6g}, $4f^{10}$ $\{5d^2, 6s^2, 5d6s, 5d6p, 6s6p\}$.

As observed in the case of Nd II, U II and U III in [13], the ground level predicted by HFR with such model does not match the observed one. In the present case of our HFR calculation for Er III, the computed ground level belongs to the $4f^{11}5d$ configuration (with $J = 6$) and is thus different from the observed one, $4f^{12}\ {}^3H_6$ [33]. However, as mentioned by Flörs et al. [13] and as formally shown by Deprince et al. [34] in the case of U II and U III, the impact of this level inversion problem has only a minor effect on the computed atomic opacities. Nevertheless, similarly to our previous work about U II and U III [34], a calibration procedure was tested for our Er III HFR data to discuss the impact of consider-

Table 1 Parameters of the statistical distribution of energy levels, $D_C(E)$, i.e., average energy, E_{av}, standard deviation, $\sqrt{v_C}$, and total number of levels, N_C, for each configuration considered in Er III, as taken into account in our statistical RTA calculation

Configuration	E^a_{av} [cm^{-1}]	$\sqrt{v_C}^b$ [cm^{-1}]	N^c_C
$4f^{12}$	26016	15704	13
$4f^{11}5f$	139892	25721	523
$4f^{11}6f$	162946	25716	523
$4f^{11}6p$	81298	25801	254
$4f^{10}6s^2$	135634	34272	110
$4f^{10}5d^2$	109312	35916	4339
$4f^{10}5d6s$	116256	35154	2019
$4f^{11}5d$	42975	26279	397
$4f^{11}6d$	128256	25710	397
$4f^{11}5g$	163485	25712	615
$4f^{11}6g$	175625	25712	615
$4f^{11}6s$	43045	25664	86
$4f^{10}5d6p$	156324	35340	5885
$4f^{10}6s6p$	171783	36050	1225

[a] HFR configuration average energy (see Sect. 2.3)
[b] Computed using HFR radial integrals and the compact formulae tabulated in Bauche et al. [26] (see Sect. 2.3)
[c] Computed using Eq. (2) in Carvajal Gallego et al. [27] (see Sect. 2.3)

ing improved atomic data in the opacity computations and assess whether such a calibration is worth considering (at least in a first attempt). In order to do that, we adjusted the average configuration energies to the one derived from observed levels given by Wyart et al. [33]. As expected, the atomic energy levels predicted by HFR were found to be much closer to the observed ones for the data set arising from the calculation including the calibration procedure, since the calibrated and the *ab initio* energy levels agree with the observed levels from [33] within 4% and 37% on average, respectively. In Sect. 3.3, we discuss the effect of considering such improved calibrated data in the computation of atomic opacities for Er III.

3.2 RTA atomic data simulation

We recently showed in Carvajal Gallego et al. [27] that the Resolved Transition Array (RTA) described in Sect. 2.3 was well suited to simulate atomic data in order to calculate opacities. Indeed, in that paper, this approach was successfully used for Sm VIII, Eu VI and Dy VIII, the latter having such a large matrix size that it was extremely challenging to diagonalize it with the Cowan's code. By simulating atomic data with this approach, we reproduced well the opacity calculated with HFR atomic data for the above-mentioned three ions. Therefore, in the present paper, we applied this RTA statistical approach to a lowly charged lanthanide ion, namely Er III, to compare the opacity estimated with method to the one calculated using HFR atomic data.

We used the same set of configurations as the one considered for HFR, which was described in Sect. 3.1. It corresponds to 22 E1 transition arrays since the electric dipole transition operator is monoelectronic. All these configurations are displayed in Table 1 where we also present a summary of the energy level distribution parameters for each configuration taken into consideration in the RTA simulation for Er III. Specifically, we give the average energy, E_{av}, the standard deviation, $\sqrt{v_C}$, and the number of levels, N_C.

In Table 2, we present our statistical RTA values for the number of lines, $L(C_l - C_u)$ and the total strength, $S(C_l - C_u)$, for each $C_l - C_u$ array in Er III. The values of the corresponding unweighted, $\sqrt{v_{un}}$, and weighted, $\sqrt{v_w}$, standard deviations of the wavenumber distribution are also reported.

Table 3 reports the statistical RTA values of the average wavenumber, σ_{av}, and the correlation parameters α and β for each $C_l - C_u$ array in Er III.

3.3 Expansion opacities

We computed the bound–bound atomic opacity of Er III for typical conditions expected in the kilonova ejecta (based on the AT2017gfo case) about 1 day after the neutron star merger, corresponding to temperatures of several thousands Kelvin and densities around 10^{-13} g cm^{-3} [35]. At this time post-merger, the kilonova ejecta is in its photospheric phase, in which LTE conditions are expected to be valid [36]. Only lowly ionized elements are present in the kilonova ejecta for such conditions, namely from the neutral to the trebly ionized species [see, e.g., 13,35]. The ionic fraction maximum of Er III is obtained at a temperature of $T = 7000$ K (similarly to Nd III as shown in [13]) under the LTE approximation, plausible with kilonova ejecta conditions one day after the merger. In this work, we thus essentially considered Er III opacity computation at this temperature.

Table 2 Statistical RTA values for the total strength, $S(C_l - C_u)$, and the number of lines, $L(C_l - C_u)$, for each $C_l - C_u$ array in Er III

$C_l - C_u$ array	$L(C_l - C_u)^a$	$S(C_l - C_u)^b$ [a.u.]	$\sqrt{v_{un}}^c$ [cm^{-1}]	$\sqrt{v_w}^c$ [cm^{-1}]
$4f^{12} - 4f^{11}5d$	1979	570.61	22692	15189
$4f^{12} - 4f^{11}5g$	2656	6.54	29087.42	20278.22
$4f^{12} - 4f^{11}6d$	1979	20.87	28735.51	19536.09
$4f^{12} - 4f^{11}6g$	2656	5.62	29087.76	20297.61
$4f^{11}5f - 4f^{11}5d$	72017	17348.6	35220.46	5367.06
$4f^{11}5f - 4f^{11}5g$	103445	379861.5	25401.45	674.81
$4f^{11}5f - 4f^{11}6d$	72017	3762886.4	23228.47	838.19
$4f^{11}5f - 4f^{11}6g$	103445	11154.80	27896.50	721.40
$4f^{11}6p - 4f^{11}5d$	37118	11154.80	28401.92	4964.07
$4f^{11}6p - 4f^{11}6s$	8393	8316.96	27905.95	2429.05
$4f^{11}6p - 4f^{11}6d$	37118	34673	29794.50	2129.36
$4f^{11}6p - 4f^{10}5d6p$	475651	9525.79	37704.39	18097.20
$4f^{11}6f - 4f^{11}5d$	72017	5041.93	35417.91	5489.90
$4f^{11}6f - 4f^{11}5g$	103445	199453.44	22511.09	466.82
$4f^{11}6f - 4f^{11}6d$	72017	20183.65	27616.31	916.06
$4f^{11}6f - 4f^{11}6g$	103445	583872.3	23408.83	419.09
$4f^{10}6s^2 - 4f^{10}6s6p$	48569	20500.48	36027.24	3158.97
$4f^{10}5d^2 - 4f^{11}5d$	574415	14411.66	29342.05	18931.09
$4f^{10}5d^2 - 4f^{10}5d6p$	8168336	14411.66	24598.57	6069.55
$4f^{10}5d6s - 4f^{11}6s$	61183	3162.93	40278.38	19827.61
$4f^{10}5d6s - 4f^{10}5d6p$	3884483	216698.4	38106.15	3855.46
$4f^{10}5d6s - 4f^{10}6s6p$	854513	43012.25	40332.37	8530.42

[a] Calculated using Eq. (8) (see Sect. 2.3)
[b] Calculated using Eq. (10) (see Sect. 2.3)
[c] Evaluated using the compact formulae of Bauche-Arnoult et al. [29,30] (see Sect. 2.3)
The corresponding unweighted, $\sqrt{v_{un}}$, and weighted, $\sqrt{v_w}$, standard deviations of the wavenumber distribution are also given

In this study, we focused on the widely used expansion opacity [37–39], which is given by

$$\kappa_{\exp}(\lambda) = \frac{1}{ct\rho} \sum_l \frac{\lambda_l}{\Delta\lambda} \left(1 - e^{-\tau_l}\right), \tag{14}$$

where t is the time post-merger, ρ is the ejecta density, $\Delta\lambda$ is the wavelength bin width and λ_l is the radiative wavelength whose Sobolev optical depth is defined by [40] as

$$\tau_l = \frac{\pi e^2}{m_e c} f_l n_l \lambda_l t, \tag{15}$$

in which f_l is the oscillator strength of the line with wavelength λ_l related to the corresponding lower level number density n_l. The number densities of the lower levels can be computed under the LTE assumption by using the Saha and Boltzmann equations as detailed by Carvajal Gallego et al. [41].

In this work, the bin width was chosen to be 1% of the wavelength to smooth the curves, while it does not affect neither the absolute scale nor the shape of the expansion opacities. The Sobolev approximation [40] is justified to compute opacities in the expansion formalism for NSM ejecta in light of the high expansion velocities ($\approx 0.1c$) of the latter [13].

The expansion opacity of Er III was thus computed for the above-mentioned conditions (t = 1 day post-merger, T = 7000 K and $\rho = 10^{-13}$ g cm^{-3}) using both the *ab initio* (uncalibrated) and the calibrated set of `HFR` atomic data detailed in Sect. 3.1. Both computed Er III opacities are displayed in Fig. 1. It can be noticed on this figure that the expansion opacity obtained using the calibrated data is close to the one determined with the uncalibrated data, even if the accuracy of the latter is poorer as explained in Sect. 3.1. This confirms the conclusion made by Deprince et al. [34] for U II and U III, i.e., the calibration of the configuration average energies that solves the level inversion problem (which notably affects the ground state) has only a minor effect on the computed expansion opacity, especially in light of the uncertainties affecting the determination of the conditions within the kilonova ejecta. In the present case, the Er III atomic opacity calculated with the uncalibrated data underestimates by about 10% on average the expansion opacities obtained with the calibrated data, while a larger difference (15–20%) affects the low wavelength range (as observed in the case of U II and U III as well in [34]), which is by the way a region of less interest for kilonova spectral modeling since far UV wavelengths (typically $\lambda \leq 2000$ Å)

Table 3 Statistical RTA values for the average wavenumber, σ_{av}, and the correlation parameters, α and β, for each $C_l - C_u$ array in Er III

$C_l - C_u$ array	σ^a_{av} [cm^{-1}]	α^b	β^c [cm]
$4f^{12}$ – $4f^{11}5d$	28244	-0.55	-4.75E-5
$4f^{12}$ – $4f^{11}5g$	136747	-5.38	-3.32E-5
$4f^{12}$ – $4f^{11}6d$	103290	-3.88	-3.61E-5
$4f^{12}$ – $4f^{11}6g$	148917	-5.53	-3.31E-5
$4f^{11}5f$ – $4f^{11}5d$	96932	1.01	-2.56E-4
$4f^{11}5f$ – $4f^{11}5g$	23522	5.09	-1.56E-3
$4f^{11}5f$ – $4f^{11}6d$	11699	4.69	-1.35E-3
$4f^{11}5f$ – $4f^{11}6f$	35661	7.42	-1.30E-3
$4f^{11}6p$ – $4f^{11}5d$	38266	1.09	-2.74E-4
$4f^{11}6p$ – $4f^{11}6s$	38321	2.99	-5.76E-4
$4f^{11}6p$ – $4f^{11}6d$	46991	3.14	-6.59E-4
$4f^{11}6p$ – $4f^{10}5d6p$	85787	-2.76	-5.75E-5
$4f^{11}6f$ – $4f^{11}5d$	119922	-0.24	-2.49E-4
$4f^{11}6f$ – $4f^{11}5g$	571	4.47	-1.63E-3
$4f^{11}6f$ – $4f^{11}6d$	34681	2.55	-1.32E-3
$4f^{11}6f$ – $4f^{11}6g$	12672	5.55	-1.55E-3
$4f^{10}6s^2$ – $4f^{10}6s6p$	53538	2.14	-4.43E-4
$4f^{10}5d^2$ – $4f^{11}5d$	67819	-2.93	-4.05E-5
$4f^{10}5d^2$ – $4f^{10}5d6p$	48654	-1.67	-2.15E-5
$4f^{10}5d6s$ – $4f^{11}6s$	82995	-1.84	-5.16E-5
$4f^{10}5d6s$ – $4f^{10}5s6p$	40260	-0.03	-3.62E-4
$4f^{10}5d6s$ – $4f^{10}6s6p$	55850	-0.89	-1.56E-4

[a] Determined for each UTA through compact formulae of [26] (see Sect. 2.3)
[b] Evaluated using Eq. (13) for each UTA (see Sect. 2.3)
[c] Evaluated using Eq. (12) for each UTA (see Sect. 2.3)

are below the detection range of existing UV instruments such as Swift [42]. Therefore, we can conclude that a calibration of the atomic data is not of primary importance to compute expansion opacities in this context and could thus be neglected, at least in a first step, especially in light of the efforts required to perform such calibration and of the lack of experimental data for many ions among lanthanides and (especially) actinides, although such improvement could still be considered in more advanced works focused e.g. on the species that contribute the most to the kilonova ejecta opacity.

The expansion opacities estimated using our statistical RTA atomic data simulation (see Sect. 3.2) for typical kilonova ejecta conditions 1 day post-merger, i.e., $\rho = 10^{-13}$ g cm^{-3}, and $T = 7\,000$ K as well as $T = 10\,000$ K, are also displayed in Figs. 2 and 3, respectively, and are compared with the corresponding expansion opacities determined using the atomic data produced by the `HFR` method (see Sect. 3.1) with and without configuration interaction (CI) (i.e., all the Slater integrals [22] between the different configurations are set to zero in the last case). In Fig. 2, the latter are in reasonable agreement to each other, showing that the configuration interaction does not play a crucial role in this case (while it is still important to include all configurations that are essential to achieve opacity convergence as detailed by Flörs et al. [13]). However, they differ from the one deduced using the RTA data. Indeed, the latter is systematically lower by about one order of magnitude with respect to the other ones. This is mainly due to the partition functions that are computed in our RTA approach using random drawn level energies which could produce a few lowest unphysical negative energies for the ground configuration. The contribution of the latter to the partition function should rapidly drop with increasing temperature. This statement is confirmed by Fig. 3 where the agreement between our RTA opacity and both `HFR` ones is recovered for a higher temperature ($T = 10\,000$ K). This unphysical effect would restrict the applicability of the present RTA approach to highly charged ions in hot plasmas (high temperatures). In order to avoid this, one could think of setting a lower limit of zero energy when drawing randomly the level energies of each configuration, which is the equivalent of the higher limit (ceiling) of the transition amplitudes in each transition array used by Gilleron et al. [43] in their RTA simulations. Nevertheless, this is out of the scope of the present work.

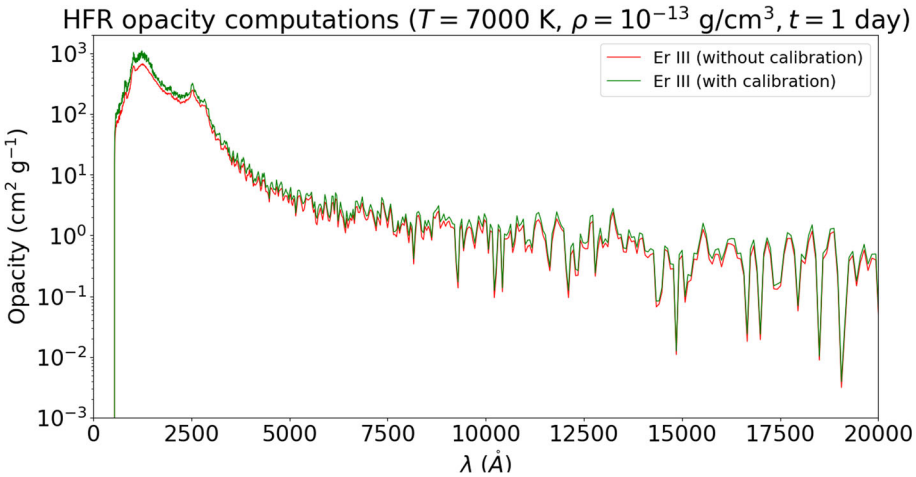

Fig. 1 Expansion opacities of Er III (for $t = 1$ day post-merger, $\rho = 10^{-13}$ g cm^{-3} and $T = 7\,000$ K) computed using the atomic data obtained by the HFR method, with and without an average configuration energy calibration procedure

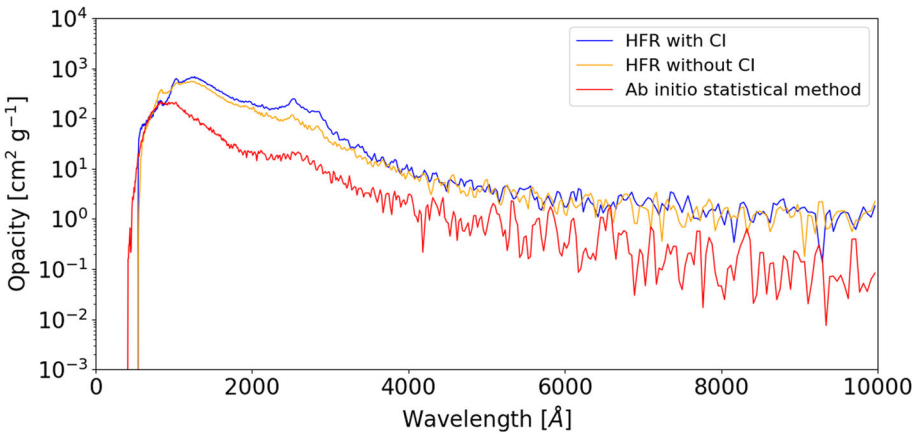

Fig. 2 Expansion opacities of Er III (for $t = 1$ day post-merger, $\rho = 10^{-13}$ g cm^{-3} and $T = 7\,000$ K) using the atomic data computed by the HFR method with configuration interaction (CI) (blue curve), calculated by the HFR method without configuration interaction (CI) (orange curve), and simulated by the statistical RTA method (red curve)

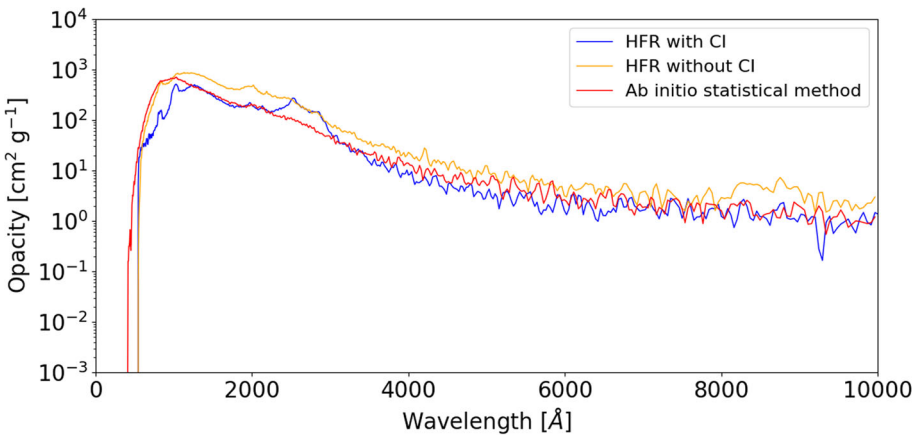

Fig. 3 Expansion opacities of Er III (for $t = 1$ day post-merger, $\rho = 10^{-13}$ g cm^{-3} and $T = 10\,000$ K) using the atomic data computed by the HFR method with configuration interaction (CI) (blue curve), calculated by the HFR method without configuration interaction (CI) (orange curve) and simulated by the statistical RTA method (red curve)

Table 4 Comparison between the available experimental energy levels within the $4f^{12}$ ground configuration of Er III and the calculated values obtained in the present work using the HFR and the MCDHF methods

Term[a]	J	E_{Exp}[a]	E_{HFR}[b]	E_{MCDHF}[b] SR	VV1	VV2	VV3	VV4	VV4+CV
^{3}H	6	0.00	0	0	0	0	0	0	0
^{3}F	4	5081.77	5148	6340	5945	5982	5885	5879	5690
^{3}H	5	6969.80	7109	6673	6762	6795	6809	6811	6807
^{3}H	4	10785.51	11042	11096	10980	10983	10989	10987	10850
^{3}F	3	12472.55	13167	14171	13681	13597	13592	13584	13202
^{3}F	2	13219.80	14027	15592	14977	14859	14844	14833	14354
^{1}G	4	18383.59	18237	18403	18291	18366	18386	18388	18341

[a] Spectroscopic designations and energies from [33]
[b] This work

Table 5 Forbidden transitions in the $4f^{12}$ ground configuration of Er III

λ_{vac}[a]	Transition	gA (HFR)[b]	gA (MCDHF)[b]	Rel. Diff.[c]	Type[d]
5439.634	$^3H_6 - {}^1G_4$	4.24(−2)	1.79(−2)	0.81	E2
7517.768	$^3F_4 - {}^1G_4$	8.15(+0)	1.08(+1)	−0.28	M1
8761.332	$^3H_5 - {}^1G_4$	1.44(+2)	1.15(+2)	0.22	M1
9271.699	$^3H_6 - {}^3H_4$	1.37(−2)	5.33(−3)	0.88	E2
12287.986	$^3F_4 - {}^3F_2$	3.11(−3)	1.25(−3)	0.85	E2
13161.220	$^3H_4 - {}^1G_4$	3.89(+1)	3.49(+1)	0.11	M1
13530.372	$^3F_4 - {}^3F_3$	4.14(+1)	4.29(+1)	−0.04	M1
14347.614	$^3H_6 - {}^3H_5$	9.78(+1)	9.82(+1)	0.00	M1
16917.497	$^3F_3 - {}^1G_4$	4.28(+0)	4.37(+0)	−0.02	M1
17532.356	$^3F_4 - {}^3H_4$	2.15(+1)	2.22(+1)	−0.03	M1
18172.732	$^3H_5 - {}^3F_3$	1.02(−3)	4.22(−4)	0.83	E2
19365.621	$^3F_2 - {}^1G_4$	1.88(−5)	5.23(−6)	1.13	E2
19678.183	$^3H_6 - {}^3F_4$	5.28(−4)	2.35(−4)	0.77	E2
26207.442	$^3H_5 - {}^3H_4$	9.20(+0)	1.01(+1)	−0.09	M1
41079.740	$^3H_4 - {}^3F_2$	6.24(−6)	2.71(−6)	0.79	E2
52965.260	$^3F_4 - {}^3H_5$	1.97(−1)	2.17(−1)	−0.10	M1
59275.417	$^3H_4 - {}^3F_3$	2.85(−1)	2.61(−1)	0.09	M1
133824.021	$^3F_3 - {}^3F_2$	4.22(−2)	4.34(−2)	−0.03	M1

[a] Vacuum wavelengths, in Å, deduced from the experimental energy levels [33]
[b] Sum of M1 and E2 gA-values, in s^{-1}. A(B) stands for A × 10^B
[c] Relative difference evaluated by $\Delta gA/\overline{gA}$ where $\Delta gA = gA_{HFR} - gA_{MCDHF}$ and $\overline{gA} = (gA_{HFR} + gA_{MCDHF})/2$
[d] Contributions larger than 10%

4 Kilonova nebular phase: forbidden lines

4.1 HFR calculations

In a first step, the transition probabilities for M1 and E2 lines within the $4f^{12}$ ground configuration of Er III were computed using the HFR method. All the even-parity configurations included in the physical model described in Sect. 3.1 were retained in the calculations, i.e., $4f^{12}$, $4f^{11}6p$, $4f^{11}5f$, $4f^{11}6f$, $4f^{10}5d^2$, $4f^{10}6s^2$ and $4f^{10}5d6s$. This gave rise to 18 forbidden transitions involving the 7 experimental energy levels classified by Wyart et al. [33] and listed in Table 4, as belonging to the $4f^{12}$ configuration. These lines are listed in Table 5. Note that, although the calculated energy levels were found to be in reasonable agreement with the experimental observations, as discussed in Sect. 3.1, the HFR gA-values were corrected using wavelengths deduced from the experimental energy levels observed in [33].

4.2 MCDHF calculations

In a second step, transition probabilities for [Er III] lines were computed using the MCDHF method starting with the $4f^{12}$ ground configuration as a single reference (SR) on which all the orbitals from 1 s to 4f were optimized. From this SR different physical models were investigated in order to improve the wavefunctions and the corresponding energy levels. This was done by gradually expanding our basis of configuration state functions to take valence–valence (VV) and core–valence (CV) into account. Different VV models were built by considering single and double (SD) electron substitutions from the valence 4f subshell to an active set

denoted by {ns,n'p,n"d,...}, where n, n', n",... are the maximum values of the principal quantum number (n) associated to an azimuthal quantum number (l). It was found that a good convergence was obtained when considering the successive active sets {5 s,5p,5d,5f,5 g}, {6 s,6p,6d,6f,6 g}, {7 s,7p,7d,7f,6 g} and {8 s,8p,8d,7f,6 g}, giving rise to the VV1, VV2, VV3 and VV4 models. From the latter model, CV correlations were added within a relativistic configuration interaction (RCI) framework where single and restricted double (SrD) excitations from the 5 s and 5p core orbitals to the {8 s,8p,8d,7f,6 g} active set were permitted, the term 'restricted' meaning that only a maximum of one hole was considered in the subshells of interest. This led to the VV4+CV model in which a total of 893 406 CSFs was involved when limiting the calculations to total angular momentum numbers ranging from $J = 2$ to $J = 6$.

In Table 4, the calculated energy levels deduced from the different MCDHF models are compared with the experimentally known values in the $4f^{12}$ ground configuration of Er III. When looking at this table, it is clear that the agreement between theoretical and experimental results improves with the complexity of the MCDHF model used, the mean relative deviation $\Delta E/E_{\rm Exp}$ (with $\Delta E = E_{\rm MCDHF} - E_{\rm Exp}$) being found to be equal to 0.0931 ± 0.1146, 0.0651 ± 0.0.0823, 0.0652 ± 0.0804, 0.0624 ± 0.0743, 0.0620 ± 0.0738 and 0.0420 ± 0.0547 for SR, VV1, VV2, VV3, VV4, and VV4+CV models, respectively. The VV4+CV model was therefore adopted for the calculations of transition rates and, even if the experimental energy structure was well reproduced with this model, the M1 and E2 transition probabilities were nevertheless corrected using wavelengths deduced from the experimental energy levels observed by Wyart et al. [33] within the $4f^{12}$ configuration.

4.3 Transition probabilities

The transition probabilities of [Er III] lines obtained in the present work using both the HFR and the MCDHF (VV4+CV) computational approaches are listed in Table 5. All possible M1 and E2 transitions involving the experimentally known energy levels within the $4f^{12}$ ground configuration are given in this table. The wavelengths (in vacuum) were deduced from the experimental levels measured by Wyart et al. [33]. A total of 18 forbidden lines were obtained when considering the 7 experimental levels classified by the latter authors as belonging to the $4f^{12}$ configuration.

When looking at Table 5, we note that HFR and MCDHF transition probabilities show an overall good agreement with each other, the mean deviation being found to be about 40% for the whole set of 18 lines. However, this deviation is greatly reduced to 10% if we only consider the transitions with gA-values larger than 10^{-1} s^{-1}, the latter being all characterized by a largely majority M1 contribution.

It is also important to emphasize that all the Er III forbidden transitions worthy of interest are included in Table 5. Indeed, even if only 7 levels were experimentally identified among the 13 possible levels in the $4f^{12}$ configuration, the 6 remaining levels, namely $^3P_{0,1,2}$, $^1D_2$, $^1I_6$ and $^1S_0$, were predicted to range between 27000 and 73000 cm^{-1} in our HFR calculations, that is to say well above around twenty levels of the opposite parity which was found to begin at 16976.28 cm^{-1} in the experimental work of [33]. Consequently, these six experimentally unknown levels are likely to depopulate predominantly via allowed electric dipole (E1) transitions rather than forbidden (M1 and E2) transitions.

4.4 Astrophysical implications

Among the 18 [Er III] lines listed in Table 5, 50% have a relatively high transition probability. Thus, if we are interested in the wavelength region covered by the *Near Infrared Spectrograph* on board the *James Webb Space Telescope (JWST)*, i.e., 0.6–5.3 μm, we find nine lines with $gA_{\rm HFR}$-values ranging from 10^{-1} to 10^{+2} s^{-1}, these lines being located at 7517.768, 8761.332, 13161.220, 13530.372, 14347.614, 16917.497, 17532.356, 26207.442 and 52965.260 Å.

It is interesting to note that the list of nine transitions given above does not contain the [Er III] line at 19678.183 Å which was nevertheless part of the shortlist of forbidden transitions that could contribute to the broad emission features observed at ∼ 2.1 μm and ∼ 4.4 μm in T_0+29 day *JWST* spectrum of the rapidly reddening thermal transient following the gamma-ray burst GRB 230307A produced by the merger of compact objects [44]. In the latter paper, this [Er III] line was in fact assumed as being one of the candidate forbidden transitions contributing to the 2.1 μm emission feature based on the argument that erbium is expected to be one of the most abundant lanthanide elements synthesized [45–49] and on the fact that this E2 transition has an upper level of low excitation energy making it possible to have a high relative population. However, the corresponding transition probability obtained in our calculations using both theoretical methods, i.e., $gA_{\rm HFR} = 5.28 \times 10^{-4}$ s^{-1} and $gA_{\rm MCDHF} = 2.35 \times 10^{-4}$ s^{-1}, seems too weak to bring a significant contribution to the observed feature.

5 Conclusion

In this work, we gave an overview of the computations performed by the Atomic Physics and Atrophysics Unit of Mons University to bring a contribution to kilonova modeling, in both the photospheric and the nebular phases, taking the doubly charged erbium ion as a test case.

Firstly, as far as the LTE photospheric phase of the kilonova ejecta is concerned, we showed that the atomic data obtained with the HFR method implemented in the

Cowan's code can be much improved (in particular to solve level inversion problems especially involving the ground state) by a calibration procedure of the configuration average energies. However, the impact of considering HFR calibrated data in the expansion opacity determination for typical conditions expected in kilonova ejecta was found to not be significant for such atomic systems with high spectral line densities as lanthanide and actinide elements, as already discussed by Flörs et al. [13] and shown by Deprince et al. [34] for weakly charged Nd and U ions, respectively. At least in a first attempt of large-scale opacity computations for all elements possibly present within the kilonova ejecta, we can thus conclude that it is not of primary importance to perform such a calibration procedure in light of the small impact on the opacities as well as of the lack of experimental data for many lanthanide and (particularly) actinide ions. In a second step, a calibration of the HFR atomic data might potentially be performed for example for the most important elements, i.e., the elements found to be the ones that contribute the most to the total kilonova ejecta opacity, or for elements with lower spectral densities for which opacities are much more dependent on wavelength accuracy.

We also tested the statistical RTA approach in order to simulate the atomic data required to estimate the Er III opacity, since this method was successfully used by Carvajal Gallego et al. [27] for several moderately charged lanthanides. We showed that this approach has some kind of limitation at low temperature since the opacity obtained considering the RTA simulated atomic data underestimates by one order of magnitude the one computed with HFR data at $T = 7000$ K, whereas a good agreement was obtained for $T = 10\,000$ K. This limitation can be understood by the few unphysical levels of negative energies randomly drawn in the RTA approach, which leads to an overestimation of the partition functions, and whose impact becomes negligible when increasing the temperature.

Concerning the NLTE nebular phase of the kilonova ejecta, a new set of transition decay rates for M1 and E2 lines within the $4f^{12}$ ground configuration of Er III was obtained in the present work using two computational approaches based on the HFR and the MCDHF theoretical methods. The agreement between the transition probabilities deduced from these two approaches was found to be good with a relative deviation of about 10% for the strongest forbidden lines. From these new radiative data, a list of [Er III] transitions that could be detected by the *Near Infrared Spectrograph* (0.6–5.3 μm) aboard the *JWST* was established. In this study, it was found that the line at 19678.183 Å was too weak to contribute significantly to the broad emission feature observed at ~ 2.1 μm in T_0+29 day *JWST* spectrum of the rapidly reddening thermal transient following the gamma-ray burst GRB 230307A produced by the merger of compact objects. This invalidates one of the assumptions made by Gillanders et al. [44] who suggested this transition (among many others) as a potential contributor to the observed spectral profile.

Acknowledgements The present work is supported by the FWO and F.R.S.-FNRS under the Excellence of Science (EOS) programme (numbers O.0004.22 and O022818F). HCG is a holder of a FRIA fellowship. PP is Research Associate of the Belgian Fund for Scientific Research F.R.S.-FNRS. PQ is F.R.S.-FNRS Research Director. Computational resources have been provided by the Consortium des Equipements de Calcul Intensif (CECI), funded by the F.R.S.-FNRS under Grant No. 2.5020.11 and by the Walloon Region of Belgium.

Author contributions

All authors contributed equally to the paper.

Data Availability Statement This manuscript has associated data in a data repository. [Authors' comment: Data will be made available on reasonable request.]

References

1. B.P. Abbott, R. Abbott, T.D. Abbott et al., Astroph. J. Lett. **848**(2), 13 (2017)
2. D. Kasen, B. Metzger, J. Barnes, E. Quataert, E. Ramirez-Ruiz, Nature **551**, 80 (2017)
3. M.M. Kasliwal, D. Kase, R.M. Lau, D.A. Perley, S. Rosswog et al., Mon. Not. R. Astron. Soc. **510**, L7 (2022)
4. J.H. Gillanders, M.A.S. McCann, S. Smartt, C.P. Ballance, Mon. Not. Roys. Astron. Soc. **506**, 3560 (2021)
5. H. Carvajal Gallego, J.C. Berengut, P. Palmeri, P. Quinet, Mon. Not. Roy. Astron. Soc. **509**, 6138 (2022)
6. H. Carvajal Gallego, P. Palmeri, P. Quinet, Mon. Not. Roy. Astron. Soc. **501**, 1440 (2021)
7. P. Rynkun, S. Banerjee, G. Gaigalas, M. Tanaka, L. Radžiūtė, D. Kato, Astron. Astrophys. **658**, 82 (2022)
8. H. Carvajal Gallego, J.C. Berengut, P. Palmeri, P. Quinet, Mon. Not. Roy. Astron. Soc. **513**, 2302 (2022)
9. G. Gaigalas, P. Rynkun, S. Banerjee, M. Tanaka, D. Kato, L. Radžiūtė, Mon. Not. R. Astron. Soc. **517**, 281 (2022)
10. L. Radžiūtė, G. Gaigalas, D. Kato, P. Rynkun, M. Tanaka, Astrophys. J. Suppl. **248**, 17 (2020)
11. H. Carvajal Gallego, J. Deprince, J.C. Berengut, P. Palmeri, P. Quinet, Mon. Not. R. Astron. Soc. **518**(1), 332–352 (2023)
12. G. Gaigalas, D. Kato, P. Rynkun, L. Radžiūtė, M. Tanaka, Astrophys. J. Suppl. **240**, 29 (2019)
13. A. Flörs, R.F. Silva, J. Deprince, H. Carvajal Gallego, G. Leck, L.J. Shingles, G. Martínez-Pinedo, J.M. Sampaio, P. Amaro, J.P. Marques, S. Goriely, P. Quinet, P. Palmeri, M. Godefroid, Mon. Not. R. Astron. Soc. **524**(2), 3083–3101 (2023)
14. H. Carvajal Gallego, J. Deprince, P. Palmeri, P. Quinet, Mon. Not. R. Astron. Soc. **522**, 312 (2023)
15. L. Radžiūtė, G. Gaigalas, D. Kato, P. Rynkun, M. Tanaka, Astrophys. J. Suppl. **257**, 29 (2021)
16. G. Gaigalas, P. Rynkun, L. Radžiūtė, D. Kato, M. Tanaka, P. Jönsson, Astrophys. J. Suppl. **248**, 13 (2020)

17. L. Maison, H. Carvajal Gallego, P. Quinet, Atoms **10**, 130 (2022)
18. C.J. Fontes, C.L. Fryer, A.L. Hungerford, R.T. Wollaeger, O. Korobkin, Mon. Not. R. Astron. Soc. **493**, 4143 (2020)
19. S. Banerjee, M. Tanaka, D. Kato, G. Gaigalas, K. Kawaguchi, N. Domoto, arXiv:2304.05810v2 (2022)
20. S. Banerjee, M. Tanaka, D. Kato, G. Gaigalas, Astrophys. J. **968**, 64 (2024)
21. Maison, L., Palmeri, P., Quinet, P.: J. Phys. B: At. Mol. Opt. Phys. (in press) (2024)
22. R.D. Cowan, *The Theory of Atomic Structure and Spectra* (University of California Press, Berkeley, 1981)
23. I.P. Grant, *Relativistic Quantum Theory of Atoms and Molecules* (Springer, Berlin, 2007)
24. C. Froese Fischer, G. Gaigalas, P. Jönsson, J. Bieron, Comput. Phys. Commun. **237**, 184 (2019)
25. J. Bauche, C. Bauche-Arnoult, J.-F. Wyart, M. Klapisch, Phys. Rev. A **44**, 5707 (1991)
26. J. Bauche, C. Bauche-Arnoult, O. Peyrusse, *Atomic Properties in Hot Plasmas from Levels to Superconfigurations* (Springer, Berlin, 2015)
27. H. Carvajal Gallego, J.-C. Pain, M. Godefroid, P. Palmeri, P. Quinet, J. Phys. B At. Mol. Phys. **57**, 035001 (2024)
28. S.A. Moszkowski, Prog. Theor. Phys. **28**, 1 (1962)
29. C. Bauche-Arnoult, J. Bauche, M. Klapisch, Phys. Rev. A **20**, 2424 (1979)
30. C. Bauche-Arnoult, J. Bauche, M. Klapisch, Phys. Rev. A **25**, 2641 (1982)
31. R. Karazija, L. Rudzikaitė, Liet. Fiz. Rinkinys **28**, 294 (1988)
32. R. Karazija, *Sums of Atomic Quantities and Mean Characteristics of Spectra* (Mokslas, Vilnius, 1991)
33. J.-F. Wyart, J. Blaise, W.P. Bidelman, C.R. Cowley, Phys. Scr. **56**(5), 446 (1997)
34. J. Deprince, H. Carvajal Gallego, M. Godefroid, S. Goriely, P. Palmeri, P. Quinet, Eur. Phys. J. D **77**(6), 93 (2023)
35. M. Tanaka, D. Kato, G. Gaigalas, K. Kawaguchi, Mon. Not. R. Astron. Soc. **496**(2), 1369–1392 (2020)
36. Q. Pognan, A. Jerkstrand, J. Grumer, Mon. Not. R. Astron. Soc. **513**(4), 5174–5197 (2022)
37. R.G. Eastman, P.A. Pinto, J. 412, 731 (1993)
38. D. Kasen, N.R. Badnell, J. Barnes, Astrophys. J. **774**(1), 25 (2013)
39. M. Tanaka, K. Hotokezaka, Astrophys. J. **775**(2), 113 (2013)
40. Sobolev, V.V.: Moving Envelopes of Stars (1960)
41. H. Carvajal Gallego, J. Deprince, M. Godefroid, S. Goriely, P. Palmeri, P. Quinet, Eur. Phys. J. D **77**(5), 72 (2023)
42. P.W.A. Roming, T.E. Kennedy, K.O. Mason et al., Space Sci. Rev. **120**, 95 (2005)
43. F. Gilleron, J. Bauche, C. Bauche-Arnoult, J. Phys. B At. Mol. Phys. **40**, 3057–3074 (2007)
44. J.H. Gillanders, E. Troja, C.L. Fryer, M. Ristic, B. O'Connor, et al. arXiv:2308.00633 (2023)
45. S. Goriely, A. Bauswein, H.T. Janka, Astrophys. J. **738**, 32 (2011)
46. A. Bauswein, S. Goriely, H.T. Janka, Astrophys. J. **773**, 78 (2013)
47. S. Goriely, J.L. Sida, J.F. Lemaotre, S. Panebianco, N. Dubray, S. Hilaire, A. Bauswein, H.T. Janka, Phys. Rev. Lett. **111**, 242502 (2013)
48. S. Goriely, A. Bauswein, O. Just, E. Pllumbi, H.T. Janka, Mon. Not. R. Astron. Soc. **452**, 3894 (2015)
49. J.H. Gillanders, S.J. Smartt, S.A. Sim, A. Bauswein, S. Goriely, Mon. Not. Roys. Astron. Soc. **515**, 631 (2022)